

Real-time High-resolution CO₂ Geological Storage Prediction using Nested Fourier Neural Operators†

Gege Wen,^{a*} Zongyi Li,^b Qirui Long,^a Kamyar Azizzadenesheli,^c Anima Anandkumar,^{b,c} Sally M. Benson^a

Carbon capture and storage (CCS) plays an essential role in global decarbonization. Scaling up CCS deployment requires accurate and high-resolution modeling of the storage reservoir pressure buildup and the gaseous plume migration. However, such modeling is very challenging at scale due to the high computational costs of existing numerical methods. This challenge leads to significant uncertainties in evaluating storage opportunities, which can delay the pace of large-scale CCS deployment. We introduce Nested Fourier Neural Operator (FNO), a machine-learning framework for high-resolution dynamic 3D CO₂ storage modeling at a basin scale. Nested FNO produces forecasts at different refinement levels using a hierarchy of FNOs and speeds up flow prediction nearly 700,000 times compared to existing methods. By learning the solution operator for the family of governing partial differential equations, Nested FNO creates a general-purpose numerical simulator alternative for CO₂ storage with diverse reservoir conditions, geological heterogeneity, and injection schemes. Our framework enables unprecedented real-time modeling and probabilistic simulations that can support the scale-up of global CCS deployment.

Introduction

Carbon capture and storage (CCS) is an important climate change mitigation technology that captures carbon dioxide (CO₂) and permanently stores it in subsurface geological formations. It provides a tangible solution for decarbonizing hard-to-mitigate sectors and can generate negative emissions when combined with direct air capture or bioenergy technologies¹⁻³. Most integrated assessment modeling scenarios identify the large-scale global deployment of CCS as a necessity to achieve net-zero emissions by 2050^{4,5}. However, the current pace of CCS deployment has failed to meet expectations⁶. One of the critical challenges causing the delay is the uncertainties in evaluating storage prospects and injection capacities⁷. Injecting CO₂ into geological formations leads to pressure buildup and gaseous plume migration⁸. Forecasts of these dynamic responses are essential for evaluating CO₂ storage capacities and guiding engineering decisions. However, current numerical approaches for simulating the CO₂-water multiphase flow are highly computationally expensive. As a result, they are inadequate to provide rigorous computation supports that are urgently needed for accelerating CCS project deployments around the world⁷.

The modeling of CO₂ geological storage requires multiphase^{9,10}, multi-physics¹¹, and multi-scale simulations. The governing partial differential equations (PDEs) involving the multiphase variation of Darcy’s law are expensive to solve^{9,10}. CO₂ and water are immiscible and mutually soluble, requiring multi-physics simulation coupled with thermodynamics¹¹. Moreover, an especially challenging characteristic of CO₂ stor-

age modeling is that it demands both high-resolutions and extremely large spatial-temporal domains. The gaseous CO₂ plume requires resolutions as fine as one to two meters to provide reliable estimates^{12,13}. Near-well responses such as pressure buildup and the dry-out effect, i.e., evaporation of formation fluid into the gas phase, also require highly resolved grids around the injection well^{14,15}. Meanwhile, the pressure buildup can travel hundreds of kilometers¹⁶ beyond the CO₂ plume and interfere with other injection operations. Due to these multi-scale responses, many CCS-related analyses are forced to use inaccurate simulations with coarsened grid resolution¹⁷ and/or simplified physics¹⁸.

One popular approach for reducing the computational costs of numerical simulations is to use non-uniform grids. Specifically, the local grid refinement (LGR) approach¹⁹, has enabled simulations of real-world three-dimensional (3D) CO₂ storage projects, where the fine-grid responses capture the plume migration while the coarser grid responses capture the far-field pressure buildup²⁰⁻²². However, even with non-uniform grid approaches, these numerical models are still too expensive to be used for essential tasks such as site selection²³, optimization^{24,25}, and inversion²⁶, which require probabilistic or repetitive forward stimulations.

In recent years, machine learning approaches are emerging as a promising alternative to numerical simulation for subsurface flow problems²⁷⁻³¹. Machine learning models trained with numerical simulation data are usually much faster than simulators, because the inferences of machine learning models are often very cheap. However, standard machine learning methods suffer from the lack of generalization and struggle to provide accurate estimates away from the domain of their training data³². This limits the usage of machine learning in CO₂ storage modeling as it requires generalization under diverse geology, reservoir conditions, and injection schemes. A recent machine-learning framework, named neural operators^{33,34}, overcomes the generalization challenge by directly

^a Energy Sciences and Engineering, Stanford University, Stanford, 94305, CA, USA

^b Computing and Mathematical Sciences, California Institute of Technology, Pasadena, 91125, CA, USA

^c NVIDIA Corporation, Santa Clara, 95051, CA, USA

† Electronic Supplementary Information (ESI) available: Supplementary Text, Figs. S1 to S2, Tables S1 to S7, and References 1-10. See <https://www.rsc.org/suppdata/d2/ee/d2ee04204e/d2ee04204e1.pdf>

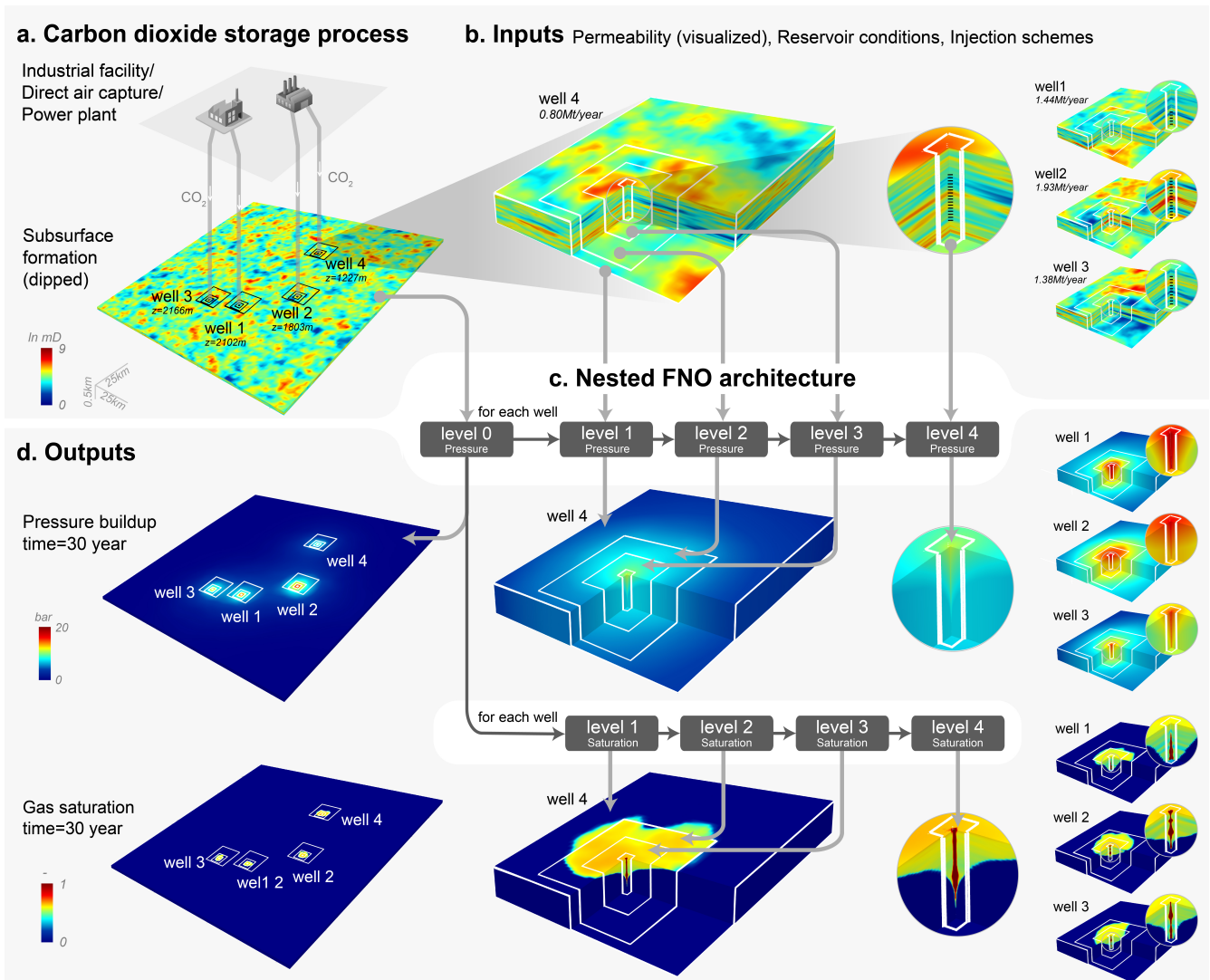


Fig. 1 Introduction to Nested-FNO. a-b. Permeability for a dipped 3D reservoir with four injection wells; white and black lines indicate level 0 to 4's boundary; the black dotted lines in the zoomed-in circles show the locations of injection perforation intervals. c. Each grey block represents an FNO model; light grey arrows point to the input and output's level; dark grey arrows show when one model's output is used as another model's input. Notice we feed level 0 pressure buildup output to level 1 gas saturation model because CO₂ plumes never migrate to level 0. d. Pressure buildup and gas saturation at 30 years.

learning the solution operator for the governing PDE family instead of single instances. Neural operators can generalize to different conditions in the PDE system as well as discretizations without the need for re-training the model.

Fourier neural operator (FNO) is a type of neural operator that offers especially remarkable predictability for flow-related problems³⁵. It uses the Fourier transform to learn the solution operator efficiently. A variant of FNO was recently proposed for predicting 2D CO₂-water multiphase flow with great generalization and accuracy³⁶. However, despite the advances in model generalization, the development of machine learning approaches for CO₂ storage is impeded by the multi-scale challenge that both high grid resolution and large spatial domain are required. Previous machine learning models are limited to either 2D problems that can only represent

flat reservoirs with a single injection well^{31,36} or 3D problems with very coarse resolutions that fail to capture essential physics^{37,38}. In real-world scenarios, CCS projects often involve multiple injection wells and dipped reservoirs. These processes can only be accurately captured by high-resolution 3D simulations, where the costs of collecting training data from numerical simulators become prohibitive.

Here we present a machine learning framework with an unprecedented capability of high-resolution dynamic 3D modeling for basin-scale CO₂ storage. We integrate the FNO machine learning architecture with a semi-adaptive LGR modeling approach for numerical simulation and present the Nested Fourier Neural Operator (Nested FNO) architecture. As shown in Figure 1, five levels of FNOs are used to predict flow responses in five different resolutions. This approach vastly re-

duces the computational cost needed during data collection as well as overcomes the memory constraints in model training. Using this approach, our prediction resolution exceeds many benchmark CO₂ storage simulations run with existing numerical models, such as Sleipner benchmark model³⁹ and Decatur model⁴⁰. Meanwhile, Nested FNO only needs less than 2,500 training data at the coarsest resolution and about 6,000 samples for the finer resolutions. Despite the small training size, it generalizes well to the large problem dimension with millions of cells and a diverse collection of practical input variables.

In addition, Nested FNO offers *real time* forecasts, where the inference speed is 700,000 times faster compared to the state-of-the-art numerical solver. The fast inference enables many critical tasks for CCS decision-making that were prohibitively expensive. For example, we present a rigorous probabilistic assessment for maximum pressure buildup and CO₂ plume footprint. Such assessment can reduce uncertainties in capacity estimation and injection designs⁸; however, it would have taken nearly two years with numerical simulators. Using Nested FNO, this assessment took only 2.8 seconds. These high-quality real-time predictions can greatly improve our ability to develop safe and effective CCS projects.

Results & Discussion

Data Overview

We consider CO₂ injection into 3D saline reservoirs⁴¹ through multiple wells over 30 years, as shown in Figure 1 a. Our data set includes a comprehensive collection of input variables for practical CO₂ storage projects, covering most realistic scenarios of potential CCS sites. Input parameters comprise reservoir conditions (depth, temperature, dip angle), injection schemes (number of injection wells, rates, perforation intervals), and permeability heterogeneity (mean, standard deviation, correlation lengths). This comprehensive data set allows the trained Nested FNO to serve as a general-purpose simulator alternative for most CCS project settings. See *Supplementary Text, Data set generation* for details on input variable sampling.

The numerical simulation data is generated using a semi-adaptive LGR approach to ensure high fidelity and computational tractability. We use global (level 0) resolution grids in the large spatial domain to mimic typical saline storage formations with infinite boundary conditions. Next, we apply four levels of local refinements (levels 1 to 4) around each well to gradually increase the grid resolutions. Going from levels 0 to 4, we reduce the cell size by 80x on the x, y dimensions and 10x on the z dimension to resolve near-well plume migration, dry-out, and pressure buildup. See *Supplementary Text* for full details on the LGR design, governing PDEs, and numerical simulation setups.

Nested FNO Architecture

The computational domain of the Nested FNO is a 3D space with time, $D = \Omega \times T$, where T is the time interval of 30 years

and Ω is the reservoir domain. We use a sequence of FNO models to predict the 3D reservoir domain consisting of subdomains Ω_i at levels 0 to 4 (Figure 1). At each refinement level, we extend the original FNO³⁵ architecture into 4D to produce outputs for pressure buildup (P) and gas saturation (S) in the 3D space-time domain. See *Supplementary Text, Fourier Neural Operator* for detailed architecture and parameters.

The input for each model includes the permeability field, initial hydro-static pressure, reservoir temperature, injection scheme, as well as spatial and temporal encoding. In CO₂ storage, pressure buildup travels significantly faster than gas saturation. Therefore, as shown in Figure 1 c, we first use an FNO model to predict the pressure buildup at level 0 to capture the global propagation as well as the interaction between wells. We then feed level 0 pressure buildup predictions around each injection well ($\hat{P}_{\Omega_0|well_j}$) to the FNO models on level 1. Each subsequent model takes the input on domain Ω_i together with the coarser-level prediction of \hat{P} or \hat{S} on Ω_{i-1} , and outputs the predictions of \hat{P} or \hat{S} on Ω_i . By giving the coarser-level prediction to the finer-level model as an input, we also provide the boundary conditions of the finer-level subdomain, which significantly improves the finer-level predictions.

CO₂ Plume Predictions

The migration of CO₂ plume is governed by the complex interplay of viscous, capillary, and gravity forces. As shown in Figure 1 a, CO₂ plumes tend to migrate up-dip due to buoyancy. They can also form distinctively different shapes and sizes according to different injection rates, perforation intervals, and permeability heterogeneity. The reservoir conditions, i.e., initial hydro-static pressure and temperature, determine CO₂ and water fluid properties, which also influence the plume migration. Due to the presence of the dip angle, reservoir conditions can vary significantly even in the same basin (Figure 1 a).

As shown in Figure 2 a, Nested FNO successfully captures all of these complex processes. The shapes and saturation distribution of each plume are accurately predicted for each well. Near the injection perforation interval, we observe dry-out zones where the gas saturation is almost one. Dry-out may cause the precipitation of salt in saline formations and can lead to potential loss of permeability and injectivity^{14,42}. Such processes are neglected by many numerical models as they require high grid resolutions and full physics simulations. Nevertheless, Nested FNO predicts the dry-out zone with excellent accuracy. We observe slightly more errors at the edges of gaseous plumes and dry-out zones; this is because the numerical simulation training data around discontinuous saturation transitions consist of inherent numerical artifacts that are less systematic.

Overall, Nested FNO displays great generalization with small overfitting (Figure 2 d). The average saturation error (δ_s) for the gaseous CO₂ plume is 1.2% for the training set and 1.8% for the testing set. See *Experimental* for the defi-

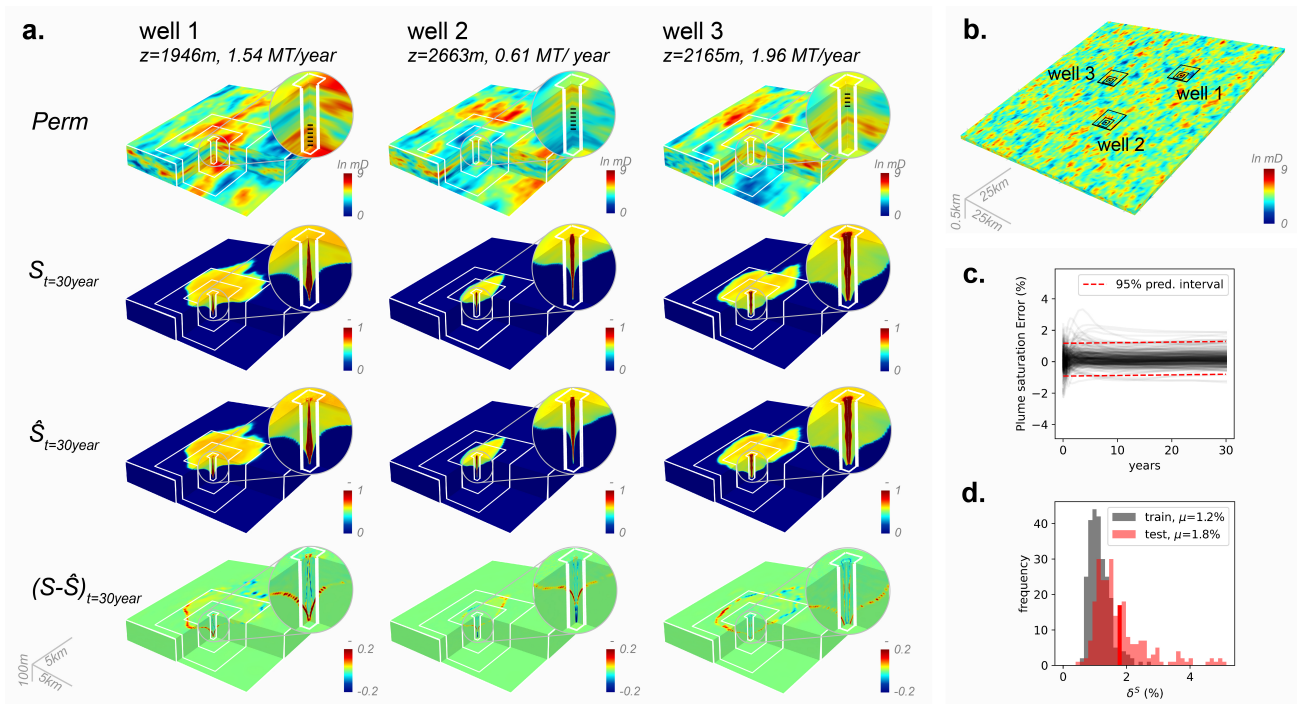


Fig. 2 Gas saturation prediction. a. Visualizations of gas saturation predictions at 30 years for a 3-well case. Each row shows permeability, gas saturation ground truth, prediction, and error. The white lines indicate the boundary between each level. b. Reservoir permeability and the location of each well. c. Testing set plume saturation error versus time for 250 random cases. The red dotted line shows the 95% prediction bands of the error. d. Error histograms for 250 cases in the training and test set. The solid red column indicates the error for the example shown in a.

nition of the evaluation metric δ_S . This accuracy is well sufficient for most practical applications, such as estimating sweep efficiencies as well as forecasting plume footprints for land acquisition or monitoring program design.

Near-well and Far-field Pressure Buildup Predictions

For basin-scale CCS projects, pressure buildups caused by different injection activities can interfere with one another. As demonstrated in Figure 3, Nested FNO precisely captures the local pressure buildup responses around each well, as well as the global interaction among them. The high resolution refinements provide accurate estimates of the maximum pressure buildup, which is an essential indicator of reservoir integrity. The global level prediction provides the spatial extent of the region of pressure buildup influence, another important parameter required for regulatory purposes⁴³. Additionally, Figure 3 a-c shows that accuracy is consistent across different resolutions and throughout the injection period. These predictions are sufficient to guide important engineering decisions, such as choosing injection rates.

The relative pressure buildup error δ^P (as defined in *Experimental*) for the training and the testing set are 0.3% and 0.5%, respectively. Similar to the gas saturation, we observe small overfitting from the error histogram (Figure 3 d) for the training and testing set. This generalization is remarkable, considering the small training data size for this high-dimensional

problem. The generalizability is achieved through a novel fine-tuning technique which we discuss in *Experimental*.

Computational Speed-up

Once Nested FNO is trained, the diverse input range allows it to act as a computationally efficient alternative to simulators. Users can skip traditional simulations and directly obtain high-fidelity and high-resolution predictions by inferring the trained machine learning models³¹. Our approach differs from the task-specific “surrogate” modeling approach^{27,29,44}, which only considers a specific set of reservoirs for a certain use case.

We analyze the computational speedup by comparing the Nested FNO’s prediction time to the numerical simulation run time of a state-of-the-art full-physics simulator ECLIPSE⁴⁵. Nested FNO’s prediction time varies from 0.025s to 0.085s depending on the number of injection wells. On average, the Nested FNO provides 400,000 (1-well case) to 700,000 (4-well case) times speedup compared to ECLIPSE. Refer to *Supplementary Text, Speedup analysis* for detailed specifications for each method.

Probabilistic Assessment

Nested FNO’s fast prediction speed enables rigorous ensemble modeling and probabilistic assessments that were previously unattainable. As an example, we conducted a probabilistic as-

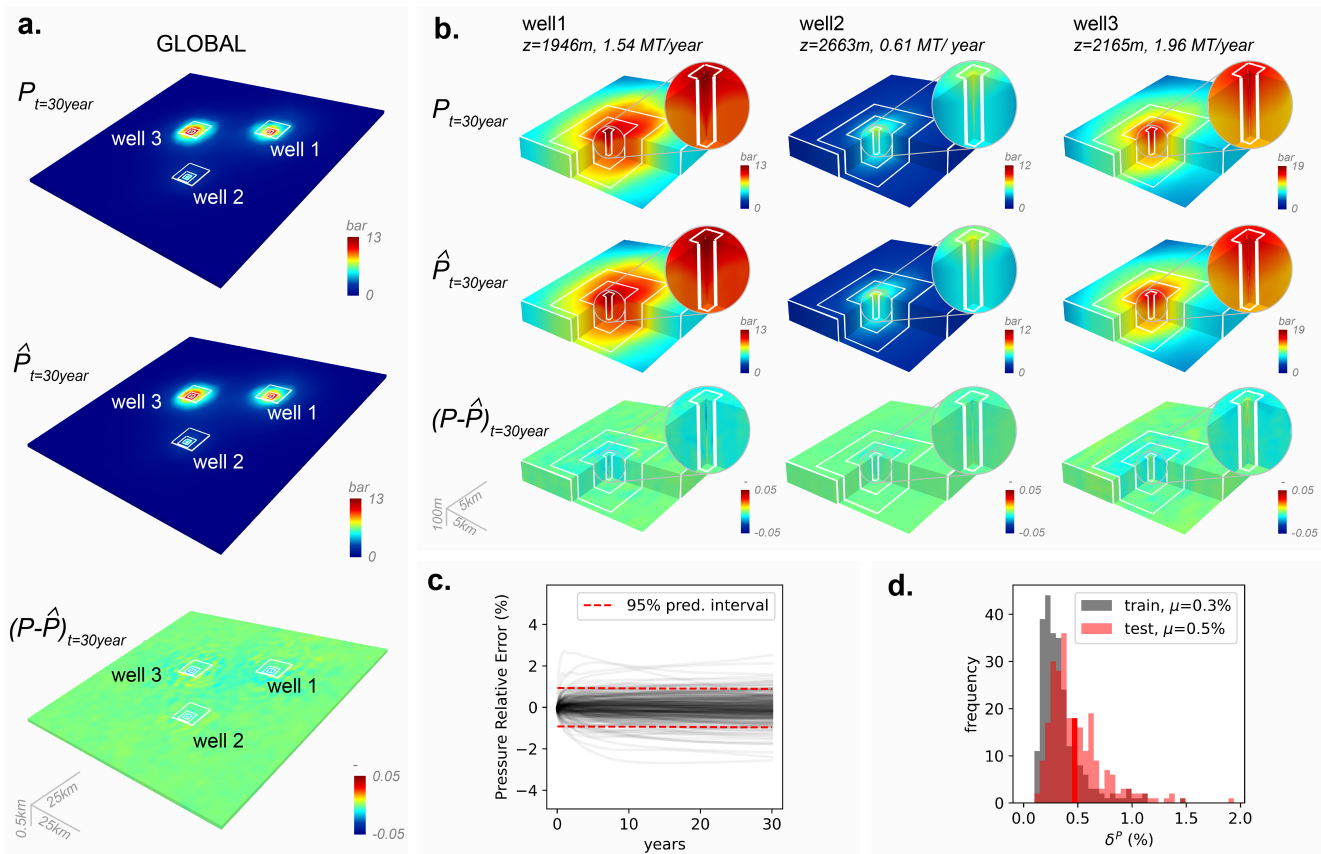


Fig. 3 Pressure buildup prediction. a. Global and b. well pressure buildup predictions at 30 years. Each row shows pressure buildup ground truth, prediction, and relative error. The white lines indicate the boundary between each level. c. Testing set pressure relative error versus time for 250 random cases. The red dotted line shows the 95% prediction bands of the error. d. Error histograms for 250 cases in the training and test set. The solid red column indicates the error for the visualized example.

assessment for the maximum pressure buildup and CO₂ plume footprint for a four-well CCS project where each well injects at a 1MT/year rate. To investigate the influence of permeability heterogeneity, we generate 1,000 realizations using a fixed set of distribution and spatial correlations, then use Nested FNO to predict gas saturation plumes and pressure buildup for each realization. Refer to *Supplementary Text, Probabilistic assessment* for detailed setups. As shown in Figure 4, we obtained probabilistic estimates of the CO₂ plume footprint and maximum pressure buildup, which can help project developers and regulators manage uncertainties⁴⁶. For example, the plume footprint helps determine the area of the land lease acquisition required⁴⁷; the maximum reservoir pressure buildup helps evaluating the safety of a certain injection scheme and ensures reservoir integrity. Running this assessment takes only 2.8 seconds with Nested FNO but requires nearly two years with traditional numerical simulators.

Generalizability of FNO-typed Architectures

A highlight of the Nested FNO is its excellent generalizability. The training sizes for Nested FNO are small (2,408 for the coarsest model and 5,916 for finer models), consider-

ing the large problem dimension with millions of cells. We achieve this generalizability through (1) a novel fine-tuning technique for the nested architecture as introduced in *Experimental* and (2) the utilization of the FNO architecture. Most existing data-driven machine learning approaches for subsurface flow use a convolutional neural network (CNN)-based architecture. CNN models' local kernels and deep architectures make them prone to overfitting^{44,48-51}. Unlike CNN, FNO uses global kernels to learn an infinite-dimensional input-output mapping in the function space³⁵. As a result, using FNO greatly reduces the demand for training data; combining the FNO architecture with the semi-adaptive LGR approach makes this high-resolution dynamic 3D problem tractable.

Besides data-driven approaches, another line of work, often referred to as a physics-informed neural network, attempts to solve the governing PDE by parameterizing governing relations and initial/boundary conditions using neural networks⁵². However, these approaches have not yet shown significant advantages in computational efficiency for multiphase flow problems with heterogeneous media⁵³⁻⁵⁶. On the contrary, Nested FNO demonstrates the great potential of data-driven approaches not only for CO₂ storage but also for other environmental and energy problems that involve multi-

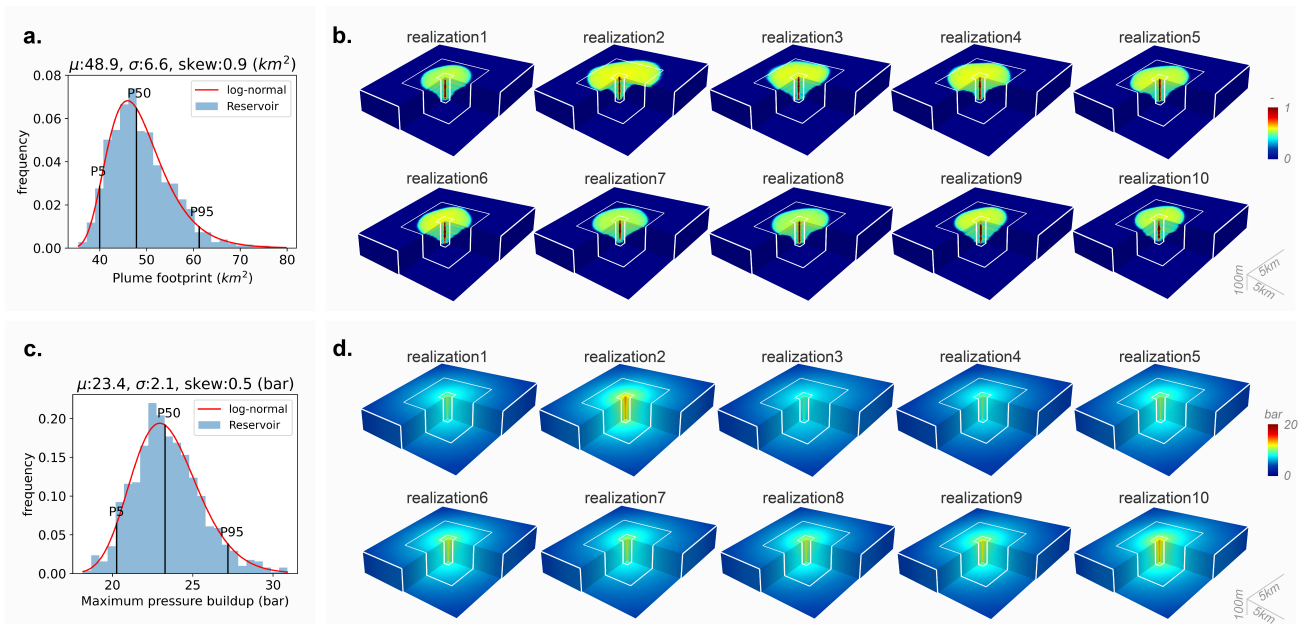


Fig. 4 Probabilistic assessment. a. Histogram of CO₂ plume footprint predictions given 1,000 permeability realizations from the same geological parameters. The result satisfies a log-normal distribution; P5, P50, and P95 are marked on the distribution. b. Ten realizations of CO₂ plume at 30 years. c. Histogram of CO₂ pressure buildup predictions given the same 1,000 permeability realizations. The result satisfies a log-normal distribution; P5, P50, and P95 are marked on the distribution. d. Ten realizations of pressure buildup at 30 years.

scale modeling. For example, in weather forecast modeling, different cyclones can develop locally while interacting with each other on a global level⁵⁷; in nuclear fusion, the collision of multiple nuclei in a particle involves long-distance interactions as well as inner-nucleus many-particle physics⁵⁸.

Conclusions

We present Nested FNO for predicting high-resolution dynamic 3D gas saturation and pressure buildup in CO₂ storage problems. The trained model provides exceptionally fast predictions and can support many tasks in the CCS deployment that require repetitive forward simulations, including but not limited to (1) probabilistic assessment - as demonstrated above, (2) site selection²³ - quick screening for a large number of potential reservoirs, (3) storage optimizations^{25,59} - exhaustive search in the parameter space, and (4) seismic inversion⁶⁰ - provide simulation outputs and gradients. Nested FNO can facilitate rigorous analyses for these tasks, therefore help reducing uncertainties and accelerate the CCS deployment scale-up progress.

In addition to providing fast and accurate forecasts, Nested FNO also promotes equity in CO₂ storage project development and knowledge adoption. This especially benefits small- to mid-sized developers⁶¹ as well as communities that desire independent evaluation of projects being proposed. High-quality forecasts were previously unattainable for these important players.

Experimental

Training procedure

The Nested FNO architecture consists of models $\mathcal{G}_{0...4}^P$ for pressure buildup and $\mathcal{G}_{1...4}^S$ for gas saturation. To train these models, we first prepare the input-output pairs for each subdomain and train each of the nine models independently. For each model, we use the ground truth numerical simulation pressure buildup and gas saturation on the coarse-level training domain to construct the input. This approach is time efficient because it allows us to train all models concurrently instead of sequentially going from coarser-level to finer-level models. Refer to *Supplementary Text, Training procedure* for full details.

Inference procedure

Once we train the nine models in the Nested FNO, we can predict the gas saturation and pressure buildup according to Algorithm 1. The inference input can be constructed given any random combination of reservoir condition (depth, temperature, and dip angle), injection scheme (number of wells, rate, location, perforation interval), and permeability field, as long as the variables are within the training data sampling ranges. Notice that the number of subdomains in Ω depends on the number of injection wells. For example, a reservoir with three injection wells has 13 subdomains $\Omega = \{\Omega_0, \Omega_{level1...4,well1}, \Omega_{level1...4,well2}, \Omega_{level1...4,well3}\}$. We repeat the inference procedure for each injection well.

Evaluation metrics

To evaluate the gas saturation prediction accuracy in reservoirs with multiple levels of refinements, we introduce the

Algorithm 1 Predict gas saturation and pressure buildup in a reservoir with n injection wells. \mathcal{G} denotes the a model, P denotes pressure buildup, S denotes gas situation, and a denotes input.

```

Use  $\mathcal{G}_0^P$  to predict  $\hat{P}_0$  given  $a_0$ 
for each well  $j = 1, \dots, n$  do
  Construct input  $(a_{1,j}, \hat{P}_0|_j)$ 
  Use  $\mathcal{G}_1^P$  and above input to predict  $\hat{P}_{1,j}$ 
  Use  $\mathcal{G}_1^S$  and above input to predict  $\hat{S}_{1,j}$ 
  for each level  $i = 2, \dots, 4$  do
    Construct input  $(a_{i,j}, \hat{S}_{i-1,j})$ 
    Use  $\mathcal{G}_i^S$  and above input to predict  $\hat{S}_{i,j}$ 
    Construct input  $(a_{i,j}, \hat{P}_{i-1,j})$ 
    Use  $\mathcal{G}_i^P$  and above input to predict  $\hat{P}_{i,j}$ 
  end for
end for

```

plume saturation error δ_S , defined as:

$$\delta^S = \frac{1}{\sum I_{t,i}} \sum_{t \in T} \sum_{i \in \Omega} I_{t,i} |S_{t,i} - \hat{S}_{t,i}|, \quad (1)$$

$$I_{t,i} = 1 \quad \text{if} \quad (S_{t,i} > 0.01) \cup (|\hat{S}_{t,i}| > 0.01).$$

S is the ground truth gas saturation, \hat{S} is the predicted gas saturation, T includes all times snapshots over the 30 years, and Ω includes all the cells as in the original domain of the numerical simulator; refer *Supplementary Text, Training procedure* for more details. We use this metric because the reservoir domain includes many cells with zero gas saturation; taking an average with these zero predictions leads to an overestimation of the gas saturation accuracy. δ_S is a more strict metric focusing on the error within the plume.

For pressure buildup, we introduce relative error δ^P :

$$\delta^P = \frac{1}{n_\Omega n_T} \sum_{t \in T} \sum_{i \in \Omega} \frac{|P_{t,i} - \hat{P}_{t,i}|}{P_{t,max}} \quad (2)$$

Here P is the ground truth pressure buildup given by numerical simulation, \hat{P} is the predicted pressure buildup, $P_{t,max}$ is the maximum reservoir pressure buildup at time t , n_Ω is the number of cells in Ω , and n_T is the number time steps. The relative error metric is commonly used for evaluating reservoir pressure buildup^{36,44}.

Fine-tuning procedure

Separate vs. sequential prediction. As described in Algorithm 1, during inference, the input for each model in levels 1 to 4 consists of \hat{S} or \hat{P} predicted by their corresponding coarser-level model. However, during training, the inputs are constructed by ground truth numerical simulation data. The discrepancy in training and inference leads to error accumulation, especially for the models that appear later in the prediction sequence.

To investigate this effect, we introduce two ways to evaluate each model: (1) separate prediction using the ground truth input taken from the numerical simulation (as in training), and (2) sequential prediction using predicted values from the

coarser level as input (as in inference). Figure 5 **a** compares the average relative pressure buildup $\delta_{\Omega_j}^P$ for each model using both separate and sequential prediction methods. Unlike δ^P , $\delta_{\Omega_j}^P$ focuses on the ability of each model to produce outputs similar to the training data, defined as:

$$\delta_{\Omega_j}^P = \frac{1}{n_T n_{\Omega_j}} \sum_{t \in T} \sum_{i \in \Omega_j} \frac{|P_{t,i} - \hat{P}_{t,i}|}{P_{t,max}}. \quad (3)$$

Figure 5 **a** shows that all models have low errors and negligible overfitting when using separate predictions. However, with sequential prediction, $\delta_{\Omega_j}^P$ quickly accumulates, going from coarser to finer-level models. The validation error of level 4 using sequential prediction increased by 13 times compared to separate predictions.

Similarly, for the gas saturation, the plume gas saturation error $\delta_{\Omega_j}^S$ for each model is defined as:

$$\delta_{\Omega_j}^S = \frac{1}{\sum I_{t,i}} \sum_{t \in T} \sum_{i \in \Omega_j} |S_{t,i} - \hat{S}_{t,i}| \quad (4)$$

$$I_{t,i} = 1 \quad \text{if} \quad (S_{t,i} > 0.01) \cup (|\hat{S}_{t,i}| > 0.01)$$

Figure 5 **d** compares $\delta_{\Omega_j}^S$ using separate verses sequential prediction. We observed less error accumulation for gas saturation than pressure buildup, which indicates that the prediction of gas saturation does not rely as heavily on coarser-level models.

Random perturbation. To reduce the error accumulation, we explored several fine-tuning techniques to improve generalizability using the level 4 pressure prediction as an example. To fine-tune \mathcal{G}_4^P , we add a perturbation to the ground truth input, $P'_{3,i} = P_{3,i} + \zeta_i$ where i represents a sample taken from the training set. We defined the coarser-level model's error in the training set as $\epsilon_3 = \hat{P}_3 - P_3$, and explore three configurations of perturbation ζ_i .

- Option 1: $\zeta_i = \epsilon_{3,j}$ - randomly sample an instance from ϵ_3 .
- Option 2: $\zeta_i = \epsilon_{3,i}$ - choose the error corresponding to the specific training sample (i.e., fine-tune with the predicted label $\hat{P}_{3,i}$).
- Option 3: $\zeta_i \sim \mathcal{N}(\mu_{\epsilon_3}, \sigma_{\epsilon_3})$ - generate a random Gaussian error using the mean and standard deviation of ϵ_3 .

As shown in Figure 5 **c**, Option 1 provides the best validation set performance with the smallest overfitting. By providing a randomly sampled noise instance from ϵ_3 with each training data, we let the finer-level models become aware of the presence of a structured error and learn to filter it out. Option 2 gives the best training set error but is significantly overfitted. Interestingly, Option 3 leads to the largest errors in both the training and validation set despite being a commonly used machine learning technique for introducing randomness.

As a result of this experiment, we applied Option 1 to \mathcal{G}_1^P , \mathcal{G}_4^P , \mathcal{G}_1^S , and \mathcal{G}_2^S . After fine-tuning, sequential prediction errors

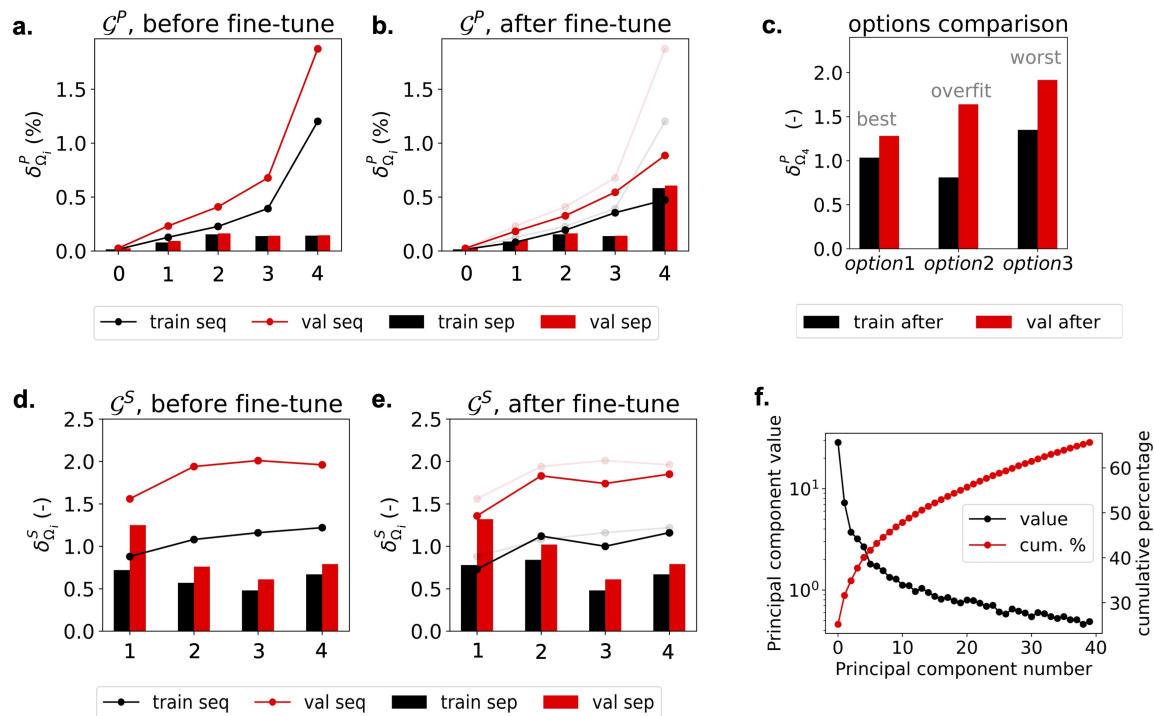


Fig. 5 Fine-tuning. Each model's separate and sequential error for a. pressure buildup before fine-tuning, b. pressure buildup after fine-tuning, d. gas saturation before fine-tuning, and e. gas saturation after fine-tuning. On the legend, 'seq' denotes sequential prediction, 'sep' denotes separate prediction. The transparent lines indicate the before fine-tune error. e. Training and validation set δ_4^P of fine-tuning using Option 1 to 3. f. Principle component number and cumulative percentage of the 40 strongest rank for \mathcal{G}_3^P 's error.

are reduced for both pressure buildup and gas saturation (Figure 5 b and e). For pressure buildup, we observe a dramatic improvement on level 4, where the validation error decreased by more than 50%.

Structure of prediction error. We hypothesize that the FNO model's predictions and errors lie in a perturbed low-dimensional manifold in the output function spaces due to its structure. To verify our hypothesis, we analyzed the functional principle components on error ϵ_3 ⁶². As shown in Figure 5 f, only a few principal components are needed to describe nearly a third of the error. Gaussian noised functions did not improve prediction because the Gaussian noise resides in an infinite-dimensional space, whereas the actual error only lives in a small linear sub-space.

Web application

The trained Nested FNO models are hosted in web application CCSNet.ai to provide real-time predictions upon the publication of this manuscript. Please also see this link for a demonstration of publicly accessible web application for our previous works.

Data and Code Availability

The python code for the Nested FNO model architecture and the data set used in training will be available at <https://github.com/gegewen/nestfno> upon the publication of

this manuscript.

Author Contributions

G.W. Conceptualization, Methodology, Software, Data acquisition, Data curation, Formal analysis, Investigation, Validation, Visualization, Writing – original draft, Writing – review & editing. Z.L. Methodology, Investigation, Validation, Writing – original draft, Writing – review & editing. Q.L. Data acquisition. K.A. Methodology, Software, Investigation, Validation, Writing – review & editing. A.A. Funding acquisition, Supervision, Writing – review & editing. S.B. Conceptualization, Formal analysis, Funding acquisition, Methodology, Resources, Supervision, Writing – review & editing.

Conflicts of interest

There are no conflicts to declare.

Acknowledgements

The authors gratefully acknowledge Yanhua Yuan from Exxon-Mobil for many helpful conversations and suggestions. G.W. and S.B. gratefully acknowledge the support by ExxonMobil through the Strategic Energy Alliance at Stanford University and the Stanford Center for Carbon Storage. Z.L. gratefully acknowledges the financial support from the Kortschak Scholars, PIMCO Fellows, and Amazon AI4Science Fellows programs. A.A. is supported in part by Bren endowed chair.

Notes and references

- 1 IEA, *Exploring Clean Energy Pathways: The Role of CO₂ Storage*, Iea technical report, 2019.
- 2 G. Luderer, Z. Vrontisi, C. Bertram, O. Y. Edelenbosch, R. C. Pietzcker, J. Rogelj, H. S. De Boer, L. Drouet, J. Emmerling, O. Fricko *et al.*, *Nature Climate Change*, 2018, **8**, 626–633.
- 3 S. Fankhauser, S. M. Smith, M. Allen, K. Axelsson, T. Hale, C. Hepburn, J. M. Kendall, R. Khosla, J. Lezaun, E. Mitchell-Larson *et al.*, *Nature Climate Change*, 2022, **12**, 15–21.
- 4 K. Riahi, D. P. Van Vuuren, E. Kriegler, J. Edmonds, B. C. O’neill, S. Fujimori, N. Bauer, K. Calvin, R. Dellink, O. Fricko *et al.*, *Global environmental change*, 2017, **42**, 153–168.
- 5 L. Cozzi, T. Gould, S. Bouckart, D. Crow, T. Kim, C. Mcglade, P. Olejarnik, B. Wanner and D. Wetzel, *World Energy Outlook 2020*, Iea technical report, 2020.
- 6 D. M. Reiner, *Nature Energy*, 2016, **1**, 1–7.
- 7 J. Lane, C. Greig and A. Garnett, *Nature Climate Change*, 2021, **11**, 925–936.
- 8 NAS, *Negative Emissions Technologies and Reliable Sequestration*, National Academies Press, 2018.
- 9 K. Pruess, C. M. Oldenburg and G. Moridis, *TOUGH2 user’s guide version 2*, Lawrence Berkeley National Lab technical report, 1999.
- 10 M. J. Blunt, *Multiphase flow in permeable media: A pore-scale perspective*, Cambridge University Press, 2017.
- 11 K. Pruess and J. Garcia, *Environmental Geology*, 2002, **42**, 282–295.
- 12 C. Doughty, *Transport in porous media*, 2010, **82**, 49–76.
- 13 G. Wen and S. M. Benson, *International Journal of Greenhouse Gas Control*, 2019, **87**, 66–79.
- 14 K. Pruess and N. Müller, *Water Resources Research*, 2009, **45**, 0043–1397.
- 15 L. André, Y. Peysson and M. Azaroual, *International Journal of Greenhouse Gas Control*, 2014, **22**, 301–312.
- 16 R. Chadwick, P. Zweigel, U. Gregersen, G. Kirby, S. Holloway and P. Johannessen, *Energy Procedia*, 2004, **29**, 1371–1381.
- 17 Z. Kou, H. Wang, V. Alvarado, J. F. McLaughlin and S. A. Quillinan, *Journal of Hydrology*, 2022, 128361.
- 18 A. Cavanagh and P. Ringrose, *Energy Procedia*, 2011, **4**, 3730–3737.
- 19 J. H. Bramble, R. E. Ewing, J. E. Pasciak and A. H. Schatz, *Computer Methods in Applied Mechanics and Engineering*, 1988, **67**, 149–159.
- 20 G. T. Eigestad, H. K. Dahle, B. Hellevang, F. Riis, W. T. Johansen and E. Øian, *Computational Geosciences*, 2009, **13**, 435–450.
- 21 B. Faigle, R. Helmig, I. Aavatsmark and B. Flemisch, *Computational Geosciences*, 2014, **18**, 625–636.
- 22 A. Kamashev and Y. Amanbek, *Energies*, 2021, **14**, 8023.
- 23 C. Callas, S. D. Saltzer, J. S. Davis, S. S. Hashemi, A. R. Kovscek, E. R. Okoroafor, G. Wen, M. D. Zoback and S. M. Benson, *Applied Energy*, 2022, **324**, 119668.
- 24 L. Nghiem, V. Shrivastava, B. Kohse, M. Hassam and C. Yang, *Journal of Canadian Petroleum Technology*, 2010, **49**, 15–22.
- 25 Z. Zhang and R. K. Agarwal, *Computational Geosciences*, 2012, **16**, 891–899.
- 26 C. W. Strandli, E. Mehnert and S. M. Benson, *Energy Procedia*, 2014, **63**, 4473–4484.
- 27 Y. Zhu and N. Zabarar, *Journal of Computational Physics*, 2018, **366**, 415–447.
- 28 S. Mo, Y. Zhu, N. Zabarar, X. Shi and J. Wu, *Water Resources Research*, 2019, **55**, 703–728.
- 29 M. Tang, Y. Liu and L. J. Durlofsky, *Journal of Computational Physics*, 2020, **413**, 109456.
- 30 G. Wen, M. Tang and S. M. Benson, *International Journal of Greenhouse Gas Control*, 2021, **105**, 103223.
- 31 G. Wen, C. Hay and S. M. Benson, *Advances in Water Resources*, 2021, 104009.
- 32 N. Kovachki, Z. Li, B. Liu, K. Azizzadenesheli, K. Bhattacharya, A. Stuart and A. Anandkumar, *arXiv preprint arXiv:2108.08481*, 2021.
- 33 Z. Li, N. Kovachki, K. Azizzadenesheli, B. Liu, K. Bhattacharya, A. Stuart and A. Anandkumar, *arXiv preprint arXiv:2006.09535*, 2020.
- 34 Z. Li, N. Kovachki, K. Azizzadenesheli, B. Liu, K. Bhattacharya, A. Stuart and A. Anandkumar, *arXiv preprint arXiv:2003.03485*, 2020.
- 35 Z. Li, N. Kovachki, K. Azizzadenesheli, B. Liu, K. Bhattacharya, A. Stuart and A. Anandkumar, *arXiv preprint arXiv:2010.08895*, 2020.
- 36 G. Wen, Z. Li, K. Azizzadenesheli, A. Anandkumar and S. M. Benson, *Advances in Water Resources*, 2022, **163**, 104180.
- 37 M. Tang, X. Ju and L. J. Durlofsky, *International Journal of Greenhouse Gas Control*, 2022, **118**, 103692.
- 38 B. Yan, B. Chen, D. R. Harp, W. Jia and R. J. Pawar, *Journal of Hydrology*, 2022, **607**, 127542.
- 39 *Data: Sleipner CO₂ reference dataset, published via the CO₂ DataShare online portal administrated by SINTEF AS*, <https://co2datashare.org/>.
- 40 *Data: Illinois State Geological Survey (ISGS), Illinois Basin - Decatur Project (IBDP) CO₂ Injection Monitoring Data, April 30, 2021. Midwest Geological Sequestration Consortium (MGSC) Phase III Data Sets. DOE Cooperative Agreement No. DE-FC26-05NT42588*.
- 41 B. Page, G. Turan, A. Zapantis, J. Burrows, C. Consoli, J. Erikson, I. Havercroft, D. Kearns, H. Liu, D. Rassool *et al.*, *The Global Status of CCS 2020: Vital to Achieve Net Zero*, 2020.
- 42 R. Miri, R. van Noort, P. Aagaard and H. Hellevang, *International Journal of Greenhouse Gas Control*, 2015, **43**, 10–21.

- 43 EPA, *Geologic Sequestration of Carbon Dioxide - Underground Injection Control (UIC) Program Class VI Well Area of Review Evaluation and Corrective Action Guidance*, 2013, 816-R-13-005.
- 44 H. Tang, P. Fu, C. S. Sherman, J. Zhang, X. Ju, F. Hamon, N. A. Azzolina, M. Burton-Kelly and J. P. Morris, *International Journal of Greenhouse Gas Control*, 2021, **112**, 103488.
- 45 Schlumberger, *ECLIPSE reservoir simulation software Reference Manual*, 2014.
- 46 R. J. Pawar, G. S. Bromhal, S. Chu, R. M. Dilmore, C. M. Oldenburg, P. H. Stauffer, Y. Zhang and G. D. Guthrie, *International Journal of Greenhouse Gas Control*, 2016, **52**, 175–189.
- 47 NETL, *Best Practices: Risk Management and Simulation for Geologic Storage Projects*, 2017.
- 48 Z. Jiang, P. Tahmasebi and Z. Mao, *Advances in Water Resources*, 2021, 103878.
- 49 H. Wu and R. Qiao, *Energy and AI*, 2020, **3**, 100044.
- 50 T. Kadeethum, D. O'Malley, J. N. Fuhg, Y. Choi, J. Lee, H. S. Viswanathan and N. Bouklas, *Nature Computational Science*, 2021, **1**, 819–829.
- 51 M. Tang, Y. Liu and L. J. Durlofsky, *Computer Methods in Applied Mechanics and Engineering*, 2021, **376**, 113636.
- 52 M. Raissi, P. Perdikaris and G. E. Karniadakis, *Journal of Computational Physics*, 2019, **378**, 686–707.
- 53 O. Fuks and H. Tchelepi, *ECMOR XVII*, 2020, pp. 1–10.
- 54 M. M. Almajid and M. O. Abu-alsaud, *Journal of Petroleum Science and Engineering*, 2021, 109205.
- 55 C. G. Fraces and H. Tchelepi, *SPE Reservoir Simulation Conference*, 2021.
- 56 E. Haghighat, D. Amini and R. Juanes, *Computer Methods in Applied Mechanics and Engineering*, 2022, **397**, 115141.
- 57 K. Dong and C. J. Neumann, *Monthly weather review*, 1983, **111**, 945–953.
- 58 S. Jin, K. J. Roche, I. Stetcu, I. Abdurrahman and A. Bulgac, *Computer Physics Communications*, 2021, **269**, 108130.
- 59 N. Kumar and S. Bryant, *SPE Annual Technical Conference and Exhibition*, 2008.
- 60 Z. Yin, A. Siahkoohi, M. Louboutin and F. J. Herrmann, *arXiv preprint arXiv:2203.14396*, 2022.
- 61 G. C. Institute, *Global CCS Institute. Special Report: Understanding Industrial CCS Hubs and Clusters*, Global CCS Institute technical report, 2016.
- 62 G. Blanchard, O. Bousquet and L. Zwald, *Machine Learning*, 2007, **66**, 259–294.